Process-induced microstructural variations in laser powder bed fusion of novel titanium alloys: A comprehensive study on volumetric energy density and alloying effects

Journal of Materials Research and Technology 31 (2024) 1430–1442

Contents lists available at ScienceDirect

Journal of Materials Research and Technology

journal homepage: www.elsevier.com/locate/jmrt

Process-induced microstructural variations in laser powder bed fusion of novel titanium alloys: A comprehensive study on volumetric energy density and alloying effects

M. Talebi [a], B. Niroumand [b,**], A. Razaghian [a], A. Saboori [c,*], L. Iuliano [c]

[a] Department of Materials Engineering, Imam Khomeini International University (IKIU), Qazvin, 3414896818, Iran
[b] Department of Materials Engineering, Isfahan University of Technology (IUT), Isfahan, 8415683111, Iran
[c] Integrated Additive Manufacturing Center, Department of Management and Production Engineering, Politecnico di Torino, Corso Duca degli Abruzzi 24, 10129, Torino, Italy

ARTICLE INFO

Handling editor: L Murr

Keywords:
Laser powder bed fusion (L-PBF)
In-situ alloying
Ti–Cu–Si alloy
Microstructure
Growth restriction factor

ABSTRACT

This study explores the effect of in-situ alloying and volumetric energy density (VED) on the microstructure of Laser Powder Bed Fusion (L-PBF) fabricated Ti alloys. Pure Ti, Ti–5Cu, and Ti–5Cu–1Si (wt%) samples were printed using elemental powders with varying VEDs. This study investigates the influence of VED and Cu/Si additions on the growth restriction factor (Q) and columnar-to-equiaxed transition of the β phase. Pure Ti samples exhibited coarse, prior columnar β grains with an average diameter of 106 μm, and a grain shape factor greater than 3.0. In contrast, both Ti–Cu and Ti–Cu–Si samples displayed a significant fraction of equiaxed prior β grains with a near-spherical morphology. Additionally, Cu/Si addition refined the prior β columnar grains, reducing their average diameter to 37 μm and 25 μm in Ti–Cu and Ti–Cu–Si, respectively. Furthermore, the study reveals a strong dependence of microstructure on VED in the Ti–5Cu–1Si alloy. Higher VED promotes a more uniform distribution of solute elements and a lower thermal gradient, resulting in finer equiaxed β grains with an average diameter of 4.9 μm, compared to samples printed at lower VEDs. The addition of Cu and Si also significantly refined the lath-like α phase and decreased the c/a ratio of the Ti HCP lattice, introducing lattice microstrains in the Ti–Cu and Ti–Cu–Si alloys. These findings demonstrate the potential of in-situ alloying and VED optimization for tailoring microstructures in novel Ti alloys fabricated via L-PBF, paving the way for achieving superior mechanical properties.

1. Introduction

Additive manufacturing (AM) is an innovative manufacturing method that builds parts incrementally, layer by layer and is a promising approach to producing parts close to the final shape. It allows the production of complex geometric objects from various structural alloys such as Ni-based superalloys, steels and functional gradient materials (FGMs) with minimal waste and short lead times [1–6]. Laser powder bed fusion (L-PBF) and electron beam powder bed Fusion (EB-PBF) methods are the two main AM technologies for the fabrication of metallic parts, which are very different in terms of their heat source, power density, and the basics of energy/material transfer [7–10]. Compared to EB-PBF, L-PBF induces higher cooling rates and, thus, faster growth rates (R) of the solidification front as well as higher thermal gradients (G) in front of the solidification front. These may lead to such problems as strong texture, residual stress, distortion, and micro-cracks [11–13]. High G leads to epitaxial growth of grains from the melt pool boundary, which is usually the dominant growth mechanism during AM processes. Accordingly, columnar grains are often observed in AM parts, which induce anisotropic mechanical properties [14]. It has been shown that by carefully adjusting such process parameters as laser power and scanning speed, it is possible to create a judicious control of the heat input, which in turn will optimize G and R to achieve the columnar to equiaxed transition (CET) phenomenon [11,15–17].

In addition to G and R, the chemical composition of the alloy is another important factor in obtaining the equiaxed structure. The effect of chemical composition on the occurrence of CET largely depends on its effect on the development of constitutional supercooling (ΔT_{CS}) in front

* Corresponding author.
** Corresponding author.
E-mail addresses: behzn@cc.iut.ac.ir (B. Niroumand), abdollah.saboori@polito.it (A. Saboori).

https://doi.org/10.1016/j.jmrt.2024.06.167
Received 27 March 2024; Received in revised form 20 June 2024; Accepted 21 June 2024
Available online 22 June 2024

of the solidification front. The effect is described as a growth restriction factor (Q) as defined by Eq. (1) for binary alloy systems.

$$Q = mC_0(1\text{-}k_0) \quad (1)$$

where m is the slope of the liquidus line, C_0 is the solute content in the alloy melt, and k_0 is the corresponding equilibrium solute partition coefficient [18–20]. Recently, Schmidt-Fetzer and Kezlov [21] proposed a more accurate method for calculating Q, which will be reviewed in section 2.

In recent years, in-situ alloying by L-PBF technology has provided a unique option for the design and synthesis of new alloys [22,23]. In-situ alloying solves the restrictions of using pre-alloyed powders and provides a low-cost solution for AM of new alloys with a wide range of chemical compositions [3]. Mosallanejad et al. [24], for example, employed in-situ L-PBF melting and alloying of a homogenous mixture of commercially pure Ti and Cu powders with average particle diameters of 29.8 and 6.6 μm, respectively, under various volumetric energy densities (VED) to produce Ti-5wt%Cu alloy. Differences in the physical and thermo-physical properties of Ti and Cu elements make their in-situ alloying by L-PBF very challenging [22,24].

It has been found that the formation of equiaxed grains in the microstructure of Ti–Cu alloy by the addition of Cu element creates superior and isotropic mechanical properties and controls the strong texture formed in the AM products [12,25]. Mereddy et al. [26] also showed that 0.75 wt%Si addition to pure Ti could significantly reduce the size of β-columnar grains in the microstructure of the components manufactured by wire arc additive manufacturing (WAAM).

Ti and its alloys have been alloys of choice for AM methods to make orthopaedic and dental implants due to their good biocompatibility, high mechanical strength, and ability to absorb laser/electron beam energy [22,27–29]. However, strong texture formation and the creation of anisotropic mechanical properties make the fabrication of such implants by AM methods challenging. Therefore, many efforts have been made to modify the microstructure and properties of AM titanium parts by adding different alloy elements such as Cu [25], Mo [30], B [31], Si [26] and W [32]. As an alloying element with a high Q factor in Ti-based alloys, Cu has a special ability to encourage the CET phenomenon [12,25]. It also improves the biological and anti-bacterial properties of Ti-based alloys used for bone replacements [23,29,33].

Based on the findings of previous researchers, it is clear that in order to achieve a fully equiaxed microstructure through AM, solidification parameters and chemical composition need to be adjusted simultaneously. For example, by using a low G resulting from the directed energy deposition (DED) process and the high Q factor of Co element, Choi et al. [34] achieved a microstructure of fully equiaxed prior β-grains during the deposition of a mixture of Ti6Al4V and Co–Cr–Mo alloy powders. With a combination of the inherent low G characteristic of the EB-PBF process and the addition of Cu element, Mosallanejad et al. [12] succeeded in AM of a fine-grained fully equiaxed Ti6Al4V7Cu alloy as well.

Mosallanejad et al. [35] also studied the effects of VED as well as Cu and B addition to pure Ti using the L-PBF method. They reported simultaneous effects of Cu and B elements on the extension of the ΔT_{CS} region and the subsequent nucleation of equiaxed grains on Ti–B precipitates as the reason for the formation of equiaxed prior β-grains.

Reviewing existing research shows that no studies have been conducted on achieving fully equiaxed microstructures in Ti–Cu alloys using the L-PBF method. As a matter of fact, there is a lack of thorough investigations into how both process factors and alloying elements affect the modification of β-columnar grains in Ti–Cu alloys produced through L-PBF. This research seeks to fill this gap by exploring the effects of factors like VED and the addition of Si on the solidification microstructure of in-situ Ti–Cu alloys made with L-PBF. The study also aims to understand the occurrence of the CET phenomenon in this alloy system.

2. Materials and methods

In this research, spherical powders of commercially pure Ti (grade 1, ≤50 μm, LPW, UK), commercially pure Cu powder (≤20 μm, Sandvik Osprey Ltd.) and commercially pure Si (≤1 μm) were mixed in a jar mill for 16 h to achieve homogeneous powder mixtures (wt%) of Ti–5Cu and Ti–5Cu–1Si compositions. A Concept Laser Mlab Cusing-R machine equipped with a 100 W fiber laser was used to print 10 × 10 × 10 mm^3 cubic sample (Fig. 1) from pure Ti, Ti–5Cu and Ti–5Cu–1Si powder mixtures under various VEDs according to Table 1.

The effective spot size of the laser beam was 50 μm, and the thickness of each layer was 25 μm for all the samples. A striping scanning strategy with 67° rotations was used to print the specimens, and the oxygen content in the building chamber was kept below 0.1%. The samples were then cut from the titanium building platform by a wire electrical discharge machine (WEDM) and sectioned along the build direction with a micro-cutter for microstructural analyses on the Y-Z cross-section.

First, the effects of Cu and Si additions on the microstructure of pure Ti were investigated using VED of 50.26 J/mm^3. Then, tests were carried out at three other different VEDs of 55.39, 64.63 and 86.36 J/mm^3 on the Ti–5Cu–1Si powder mixture to examine the effect of VED on the microstructure of the as-built samples.

The microstructures of the samples were revealed following the standard metallographic techniques and etching with Kroll's reagent (1 wt% HF, 4 wt% HNO3, and 95 wt% H2O). Optical microscopy (OM, Olympus-BX-51 M), scanning electron microscopy (SEM, Philips XL30) and field emission electron microscopy (FE-SEM, Quanta Feg 450) equipped with energy dispersive spectroscopy (EDS) device were used to investigate and analyze the microstructures. Phase analysis was performed by X-ray Diffractometer (XRD, Asenware -AW-XDM300, Cu-Kα radiation) using a step time of 1 s. Phase detection and profile fitting related to XRD patterns of Ti, Ti–5Cu and Ti–5Cu–1Si samples were carried out by PANalytical X'Pert, HighScore Plus software. Calculations related to crystallite size and microstrain of Ti, Ti–5Cu and Ti–5Cu–1Si samples were performed using the Williamson-Hall method [36].

Image J software was used to measure the average size and shape factor of the equiaxed or columnar grains and their distribution. More than 100 grains were registered for each sample. The equivalent diameter (d_{eq}) and the grain shape factor (GSF) of each grain were computed using Eqs. (2) and (3), respectively, where A (μm^2) was the area of the grain and d_1 and d_2, for a columnar grain, designate the length and width of the grain, respectively [37,38]. A large GSF corresponds to a slender columnar grain. A small d_{eq} designates a fine equiaxed grain or a narrower columnar grain.

$$d_{eq} = \sqrt{\frac{4 \times A}{\pi}} \quad (2)$$

$$GSF = d_1/d_2 \quad (3)$$

The student version of Pandat software was employed to plot non-equilibrium Scheil diagrams of the freezing ranges and to calculate the corresponding growth restriction factors (Q) according to the method proposed by Schmidt-Fetzer and Kezlov [21]. First, the corresponding solid fraction (f_s)-temperature curves for Ti–5Cu and Ti–1Si binary alloys were obtained in Scheil non-equilibrium conditions. $\Delta T_{CS} = T_L\text{-}T$ was calculated using the liquidus temperature, T_L, provided by the software data. After plotting the ΔT_{CS}-f_s curves, a second-order parabolic fit ($\Delta T_{CS} = a + b.f_s + f_s^2$) to several sampling points in very small f_s values ($0 < f_S < 0.01$) , which are usually in a temperature range of $0 < \Delta T_{CS} < 1K$, were used to measure the initial slope of the curves. Consequently, the growth restriction factor for Ti–5Cu and Ti–1Si alloys was obtained. The overall Q is the sum of the Q values for each solute element [30].

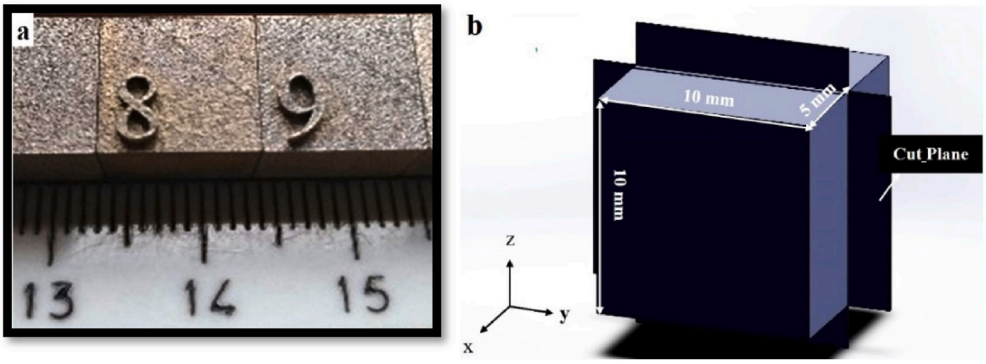

Fig. 1. a) Macrograph of some as-built Ti–5Cu–1Si cubes and b) schematic of the cross-sectioning of the samples in this work.

Table 1
The L-PBF process parameter used to build the samples in this work.

Sample	Ti	Ti–5Cu	Ti–5Cu–1Si			
VED (J/mm^3)	50.26	50.26	50.26	55.39	64.63	86.36
Scanning speed (mm/s)	700	700	700	700	600	500
Hatch Spacing (mm)	0.108	0.108	0.108	0.098	0.098	0.088
Laser Power (W)	95	95	95	95	95	95

3. Results and discussions

3.1. Microstructure analysis

Fig. 2(a) shows the optical micrograph of the pure Ti sample produced by the L-PBF process using VED of 50.26 J/mm^3.This figure shows large columnar prior β grains epitaxially grown in the build direction. The thickness of the grains varies between 60 and 90 μm, and their length reaches a few hundred micrometres. Long columnar structure formation is believed to be due to the steep G present in the L-PBF process and the lack of high-Q alloying elements [39]. Acicular-like α' phase formation is also seen as colonies in some areas of the microstructure in Fig. 2(b) as a result of rapid cooling of β phase from β transus temperature. The average width of the acicular α' phase was measured to be about 0.66 ± 0.22 μm. Similarly, a lath-like α phase with widths of 2.98–4.23 μm, as shown in Fig. 2(b)–is also formed in the microstructure of pure Ti. The optical micrograph in Fig. 2)b(reveals that the formation of lath-like α phase colonies occurred both on the prior β-columnar grain boundaries and inside the prior β-columnar grains. In addition, some irregular or close to equiaxed and elongated α grains have been formed in the microstructure, which appears as grain boundary α (α_{GB}) in some areas of the microstructure (Fig. 2(b)).

In a previous study conducted by Wysocki et al. [40], the formation of lath-like α phase and irregular or close to equiaxed α grains on the prior β grain boundaries has been reported. Fig. 2(c) shows a more detailed image of these phases at higher magnification. According to previous studies, the change in the laser scanning speed (V) leads to the

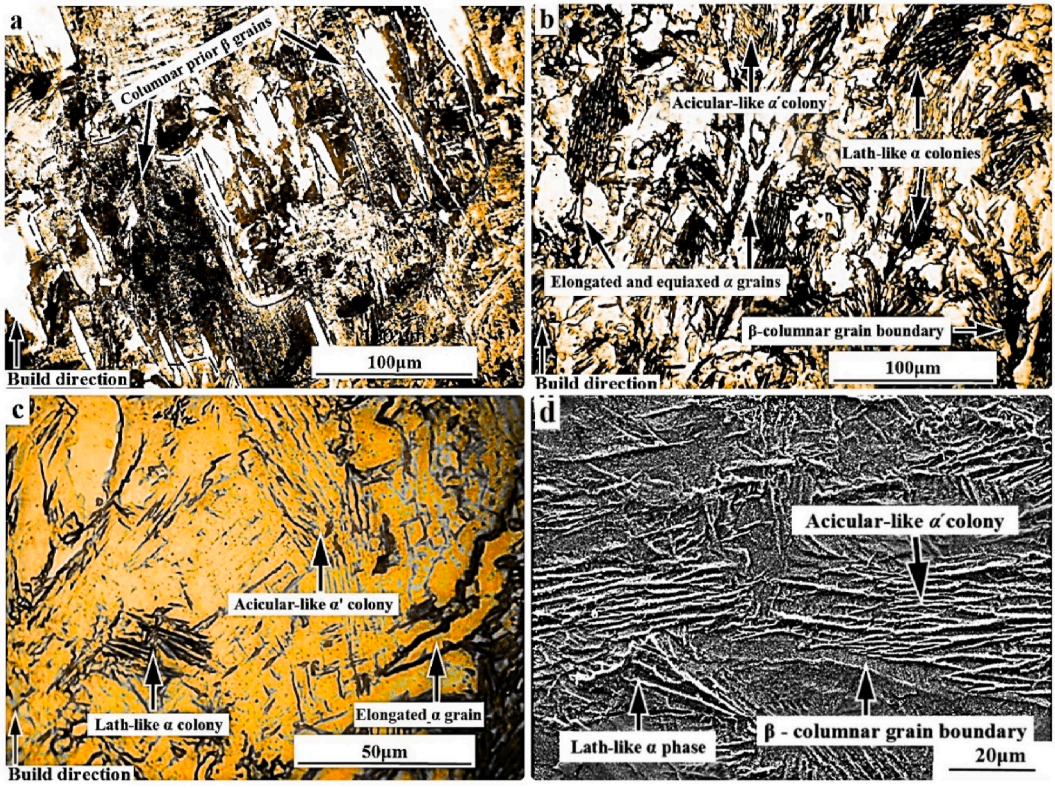

Fig. 2. a-c) OM and d) SEM micrographs of pure titanium samples produced at VED of 50.26 J/mm^3.

formation of different morphologies of α and α' phases in the microstructure of pure Ti [41,42]. For example, the transformation of coarse lath-like α phase into acicular-like α' phase has been reported by increasing V from 0.02 to 0.2 m/s under a constant laser power (P) of 100 W [42]. The underlying mechanism of this phenomenon was attributed to the different cooling rates in the L-PBF process, which is directly affected by G and V. Li et al. [41] observed the transformation of elongated and equiaxed α phase to acicular-like α' phase in the microstructure of commercially pure titanium samples fabricated by L-PBF, which occurs due to the increase of P from 50 to 250 W and also increasing in V. This means that fabrication with higher P leads to a higher G, which together with higher V lead to higher cooling rates during L-PBF process. The SEM micrograph in Fig. 2(d) points to areas very close to the prior β-columnar grains and the prior β grain boundaries where the lath-like α phase is not evident. The optical micrograph also shows these areas (Fig. 2(a)).

By examining the microstructure of the Ti–5Cu specimen made at VED of 50.26 J/mm^3 (Fig. 3(a)), the formation of equiaxed grains in some areas of the microstructure is evident. Meanwhile, the equiaxed prior β grains identified in the microstructure of the Ti–5Cu–1Si sample (Fig. 3(b)) are obviously smaller, and their number is higher in comparison to the equiaxed prior β grains of the Ti–5Cu sample (Fig. 3(a)). Considering that these samples were produced at the same VED as that of pure Ti (Fig. 2(a)), the formation of equiaxed grains in the microstructure of Ti–5Cu–1Si and Ti–5Cu samples can be due to the high potency of Cu and Si solute atoms to create large constitutional supercooling zones in front of the solidification front.

Results of image analyses in terms of the number and size of equiaxed prior β grains in the microstructure of Ti–5Cu and Ti–5Cu–1Si specimens as compared to those of the pure Ti sample are shown in the violin diagrams of Fig. 4(a). In each violin diagram, the data are divided into equal quartiles, i.e. Q1 to Q4, where 25% of the data is below Q1, 50% of the data are below Q2 (also known as the median shown by a small circle), and 75% of the data are below Q3. The distance between Q_3 and Q_1 is known as the interquartile range (IQR) and is shown by a small box in the middle of each plot. In fact, each box in Fig. 4 indicates where the main bulk of the data related to the grain size in each alloy is located. The lines extended from each box capture the range of the remaining data. If the median point is exactly in the middle of the box, the distance between Q_1 and Q_2 is equal to Q_2 and Q_3, and each line extends 1.5 times the IQR. In this situation, the data distribution is said to be symmetrical. Furthermore, in each diagram, the width of the diagram at any given grain size designates the relative number of grains corresponding to that grain size [43].

The reduction of the median value of the grain size and widening and shortening of the violin plots of Ti–5Cu and Ti–5Cu–1Si alloys in Fig. 4 (a) clearly indicates the significant grain refinement effects of addition of Cu and Si to pure Ti. In fact, Fig. 4(a) shows that the microstructure of the pure Ti sample is packed by columnar grains with grain equivalent diameters between 64 and 139 μm and a median of 106.3 μm. In the Ti–5Cu sample, with the addition of Cu, some equiaxed grains are formed, and the size of most of the grains is in the range of 6.5–55.9 μm with a median grain size of 21.2 μm. With the further addition of Si, i.e. in the Ti–5Cu–1Si sample, the number of equiaxed grains is increased, the median grain size is reduced to 11.4 μm, and the grains have smaller sizes in the range of 1–21 μm. The corresponding *GSF* violin diagrams of the samples are also shown in Fig. 4(b), which show a rapid fall in the median value of *GSF* from about 3.0 for pure Ti to about 1.0 and 1.1 for Ti–5Cu and Ti–5Cu–1Si alloys, respectively.

Despite the mentioned CET occurrence in the Ti–5Cu and Ti–5Cu–1Si alloys, some columnar grains in the microstructure of these alloys were still observed. The violin plots of the grain equivalent diameter and the *GSF* of the prior β-columnar grains in the microstructure of Ti, Ti–5Cu, and Ti–5Cu–1Si samples are shown in Fig. 4(c and d), respectively. Based on these figures, the median *GSF* of Ti, Ti–5Cu, and Ti–5Cu–1Si samples is 3.0, 3.4, and 4.9, and the median prior β-columnar grains equivalent diameter of the samples is about 106.3, 37.5 and 25.0 μm, respectively. These results indicate that while the *GFS* values of the limited number of columnar grains formed in the microstructures of Ti–5Cu and Ti–5Cu–1Si samples are somewhat larger than that of the pure Ti sample, their size is a few times smaller than those formed in the pure Ti sample.

3.1.1. *Effect of volumetric energy density (VED)*

The microstructure of Ti–5Cu–1Si alloy produced using VED of 55.39 J/mm^3 is shown in Fig. 5(a). The formation of equiaxed prior β grains with different sizes in several points of the microstructure can be seen. This difference in the grain size can be attributed to the non-uniform chemical composition and non-uniform distribution of Cu and Si elements in different areas of the microstructure. In comparison, the number of equiaxed prior β grains formed in the microstructure of the sample made at a higher VED is significantly increased (Fig. 5(b)). The increase in the density of the equiaxed prior β grains can be due to the more uniform distribution of Cu and Si elements in the microstructure as well as the lower G. Simultaneous formation of small-sized columnar grains and equiaxed grains in a single molten pool or separate molten pools, are also evident in the microstructure of the sample made at VED of 86.36 J/mm^3 (Fig. 5(c)).

For this purpose, more in-depth analyses of the chemical homogeneity of the samples was carried out using FE-SEM and EDS analyses. Distribution of Ti, Cu and Si elements in the microstructure of the Ti–5Cu–1Si samples made using the VEDs of 55.39 and 86.36 J/mm^3 as investigated by EDS line analysis are reported in Fig. 6(a and b). The extreme fluctuations of Ti, Cu and Si elements in the microstructure of

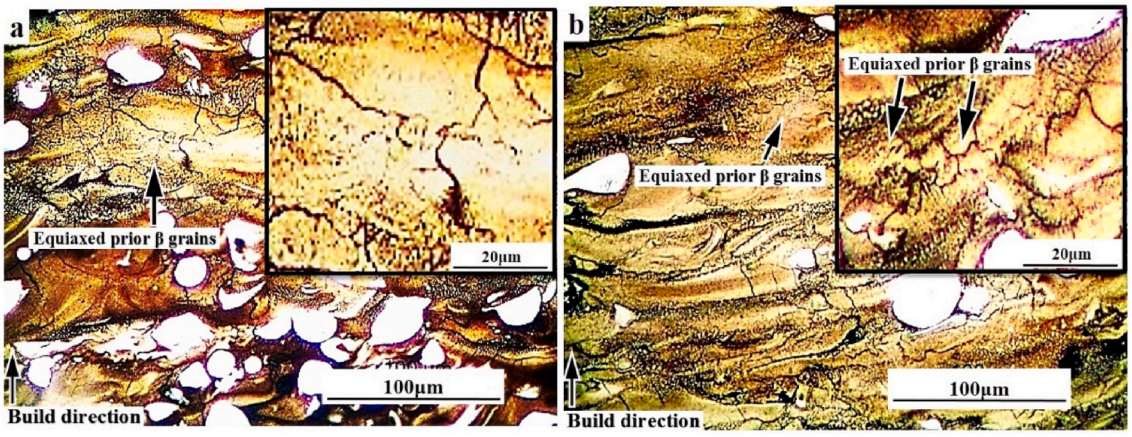

Fig. 3. Optical microstructure of a) Ti–5Cu and b) Ti–5Cu–1Si samples at VED of 50.26 J/mm^3.

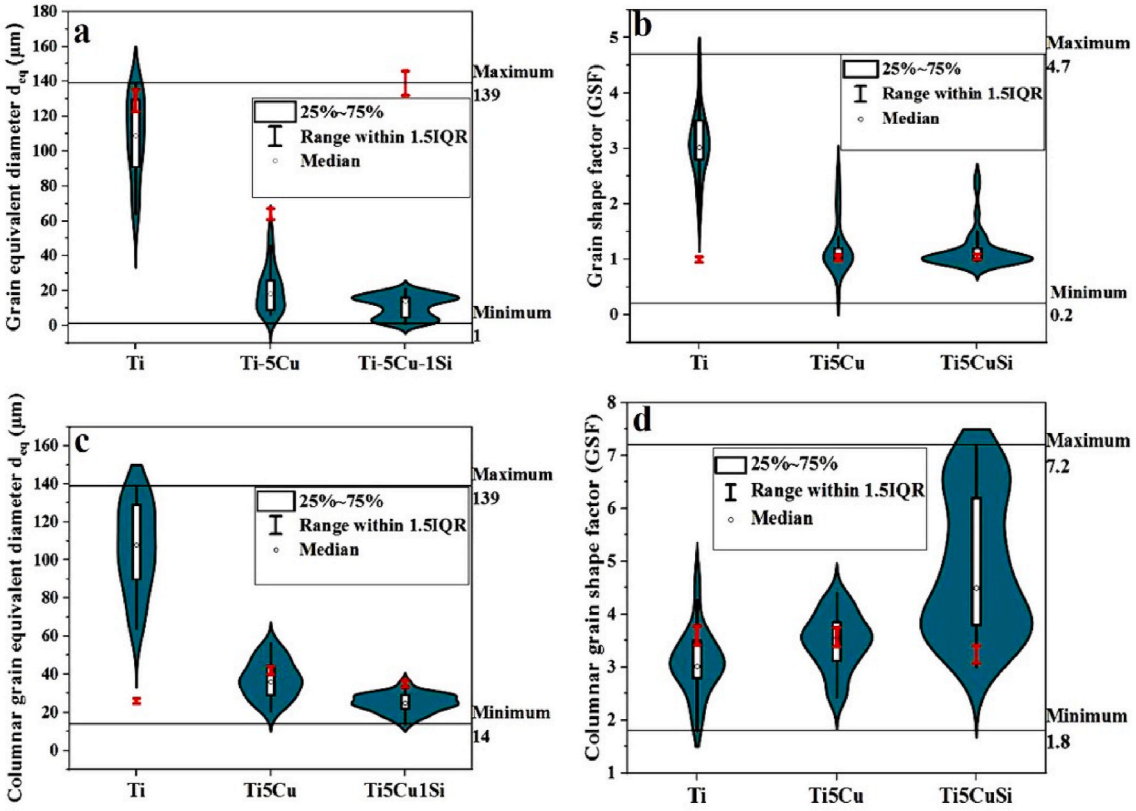

Fig. 4. Change in a) grain equivalent diameter (d_{eq}), b) grains shape factor (*GSF*), c) prior β-columnar grain equivalent diameter (d_{eq}) and d) prior β-columnar grains shape factor of different alloys (VED = 50.26 J/mm^3).

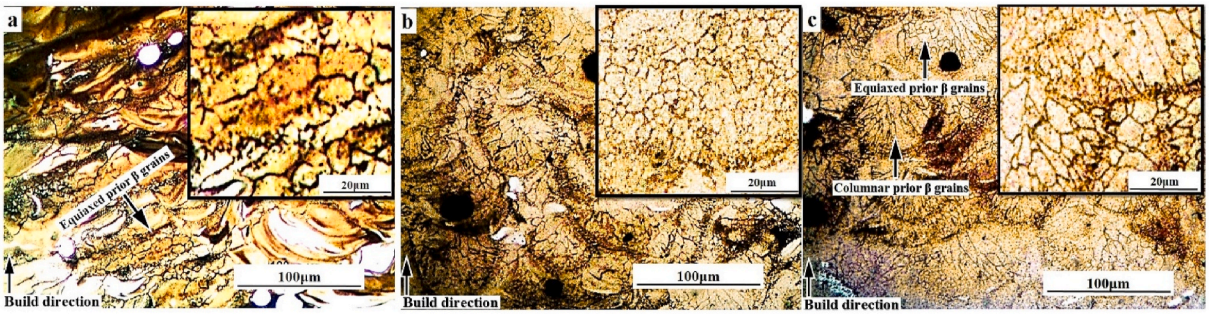

Fig. 5. Optical micrographs of Ti–5Cu–1Si sample at VED of a) 55.39 J/mm^3, b) and c) 86.36 J/mm^3.

the sample printed with the VED of 55.39 J/mm^3 (Fig. 6(a)) seems to have occurred due to incomplete mixing of elements and formation of some Cu-rich like Ti_2Cu precipitates. The distribution of Ti, Cu and Si elements in the microstructure formed at VED of 86.36 J/mm^3 is rather uniform (Fig. 6(b)).

As a general rule, higher VED or higher heat input results in the formation of larger melt pools, slower cooling rates, and lower *G* [18]. A lower *G* creates a larger ΔT_{CS} that can encourage more efficient nucleation of new grains [44]. On the other hand, the formation of finer equiaxed grains in the specimen fabricated at lower VEDs has occurred due to lower heat input and, as a result, a higher cooling rate, which provides a unique opportunity to modify the as-built microstructure [17,20,45]. A higher cooling rate and lower *G* favours the formation of equiaxed β grains. In fact, an increased cooling rate results in an increased growth rate of the solid/liquid interface (*R*). Increased *R* causes more solute segregation in front of the solid/liquid interface, which accelerates ΔT_{CS} escalation [17,20]. On the other hand, at a higher cooing rate (increased *R*), more populous but smaller heterogeneous substrates which require higher undercooling for nucleation (ΔT_n) may be activated due to the increased ΔT_{CS} [17,45].

In general, for a reasonable investigation of the solidification microstructure, the effect of not only the cooling rate but also *G* should be considered [46]. At a small *G* and cooling rate, only large heterogeneous substrates with small ΔT_n may be activated due to the small ΔT_{CS} driven by *R* [17]. In this situation, if *G* increases at a given cooling rate, activation of heterogeneous substrates will be more difficult due to the decrease of ΔT_{CS}. However, with an increase in the cooling rate at a given *G*, a larger number of substrates with larger ΔT_n are activated. This is because the thermal undercooling generated under higher cooling rate conditions facilitates nucleation on the less potent substrates requiring higher undercoolings [45].

Histograms of the average equivalent diameter (d_{eq}) distribution of prior β grains of Ti–5Cu–1Si specimens made under various VEDs are shown in Fig. 7(a–d), respectively. The average d_{eq} at VEDs of 50.26,

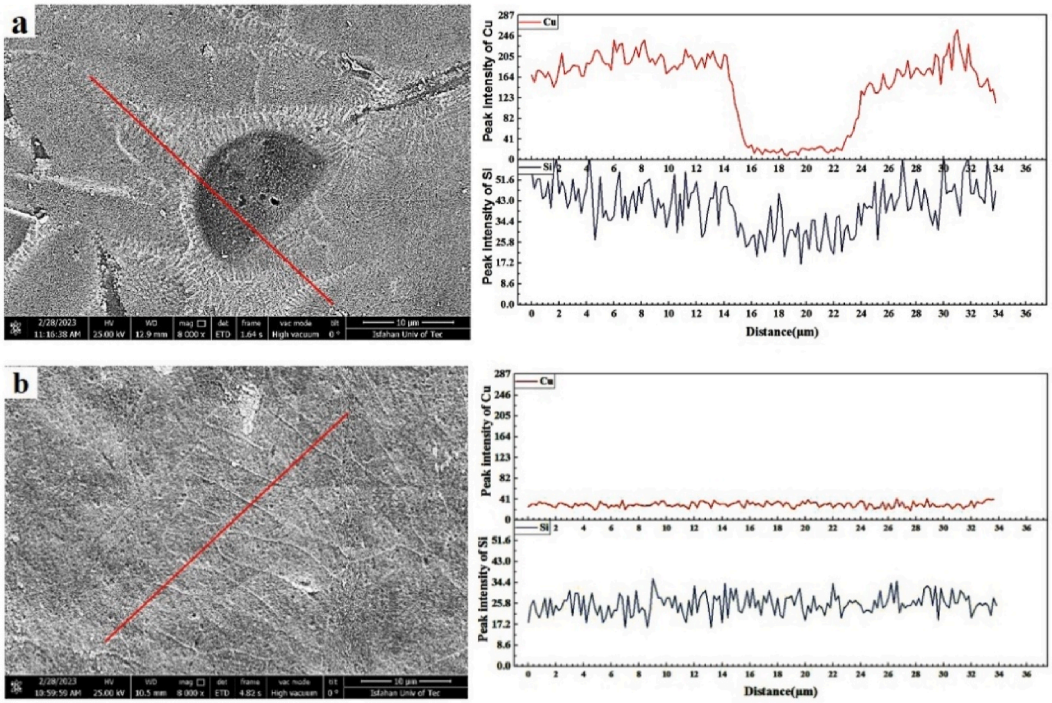

Fig. 6. FESEM micrographs and EDS line analyses of Ti–5Cu–1Si sample at VED of a) 55.39 and b) 86.36 J/mm^3.

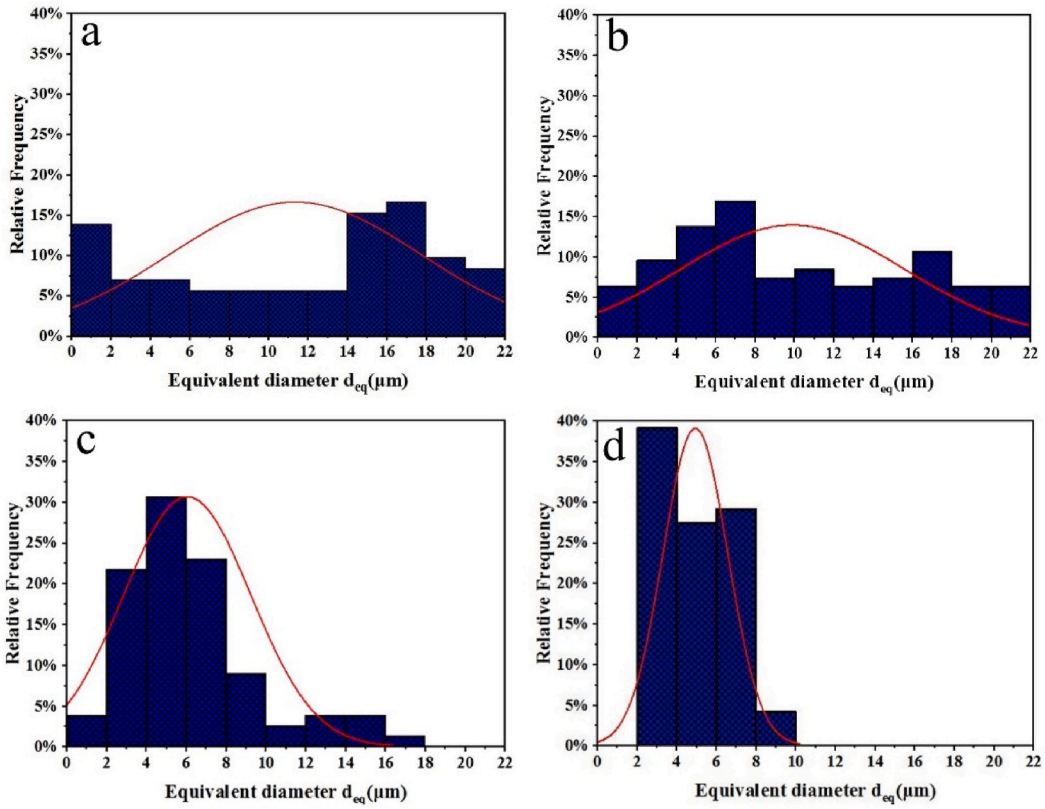

Fig. 7. Histograms of the distribution of the average equivalent diameter (d_{eq}) of equiaxed prior β grains for Ti–5Cu–1Si sample at VED of a) 50.26, b) 55.39, c) 64.63 and c) 86.36 J/mm^3.

55.39, 64.63 and 86.36 J/mm^3 was found to be about 11.4, 10.5, 6.1 and 4.9 μm, respectively. It is evident that the average d_{eq} for most of the equiaxed prior β grains of the Ti–5Cu–1Si sample at VED of 86.36 J/mm^3 is distributed in an interval between 2 and 10 μm, while the average d_{eq} distribution for the Ti–5Cu–1Si specimens produced using VEDs of 50.26 and 55.39 J/mm^3 lies in a larger interval.

Furthermore, *GSF* and d_{eq} of the columnar grains of Ti–5Cu–1Si samples as a function of VED are shown in Fig. 8. The figure shows that while *GSF* increases with VED, d_{eq} experiences a decreasing trend. This can be confirmed by comparing the shape and size of the columnar grains in the microstructure of the Ti–5Cu–1Si samples made at different VEDs (Figs. 5(c) and Fig. 9). This means that as VED increases, conditions for the formation of a large number of narrower and smaller-sized columnar prior β grains are provided. In fact, contrary to the expectations, increased VED has resulted in microstructures with finer but higher numbers of equiaxed prior β grains.

It is well documented that a high cooling rate, i.e. a characteristic condition at small VEDs, normally favours CET occurrence. In this study, however, the formation of smaller-sized equiaxed prior β grains in Ti–5Cu–1Si samples occurred at the higher VED of 86.36 J/mm^3 as compared to the samples produced at lower VEDs of 55.39 and 50.26 J/mm^3. This discrepancy is believed to be due to the more uniform distribution of Cu and Si elements (Fig. 6(b)), as well as the lower *G* due to the higher heat input. A relatively uniform distribution of Cu and Si elements at VED of 86.36 J/mm^3 would result in a uniform distribution of *Q* in the whole melt. This is thought to compensate for the smaller cooling rate induced at high heat input conditions, i.e. large VEDs.

For example, Mosallanejad et al. [12] reported a fully equiaxed structure in EBM processing of Ti6Al4V–7Cu alloy and associated this to the characteristic relatively small *G* and good elemental homogeneity of the process, which leads to a large ΔT_{CS} in the melt pool. On the contrary, due to lower laser absorbability of Cu compared to Ti [24], as well as the differences in viscosity and density of liquid Cu and liquid Ti [23,37], in-situ alloying of Ti6Al4V3Cu, Ti6Al4V1Cu, Ti5Cu, Ti6Al4V1.3Cu alloy under non-optimal L-PBF process parameters leads to the formation of local Cu-rich zones and more columnar grains formation in the as-built microstructure [22–24,47,48].

The outcomes of this work clearly demonstrated that the development of new Ti–5Cu–1Si alloy at a high VED through the in-situ alloying approach would lead to uniform distribution of Ti, Cu and Si elements in the melt pool due to higher heat input, which, along with the low *G*, provides for the formation of larger number of finer equiaxed grains compared to the samples produced at lower VEDs, e.g. 50.26 J/mm^3.

OM micrographs of Ti–5Cu–1Si and Ti samples at VED of 50.26 J/mm^3 are shown in Fig. 10. Comparing the figures clearly shows the reduced number and size of α colonies in the Ti–5Cu–1Si sample compared to those in the pure Ti sample. In the former, α colonies are limited only to scattered small, isolated areas at the boundaries of unmelted or partially melted Ti particles and on the equiaxed prior β grain boundaries. On the other hand, the formation of the α-lath phases near the titanium-rich areas is evident in higher magnification SEM micrographs of the Ti–5Cu–1Si sample, as shown in Fig. 11.

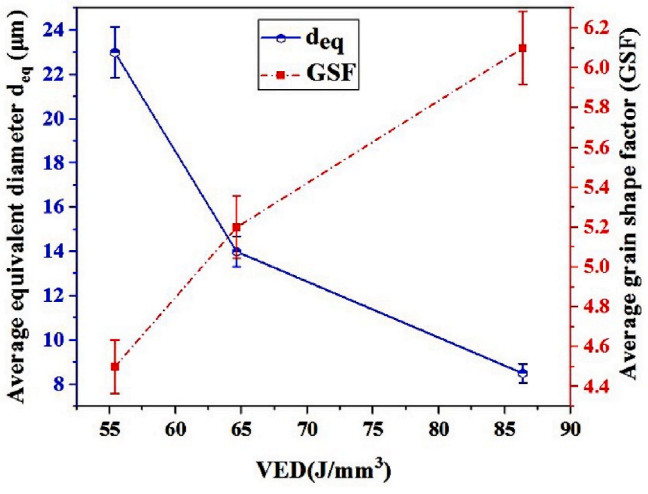

Fig. 8. Effects of VED on *GSF* and d_{eq} of the columnar prior β grains of Ti–5Cu–1Si alloy.

In order to investigate the effects of Cu and Si addition on the dimensions of the α-laths phase, the distribution histograms and average values of length, width and *GSF* of the intragranular and intergranular α-laths of the pure Ti and the Ti–5Cu–1Si samples are shown in Fig. 12 (a–f). It can be seen that the length, width and *GSF* of the α-laths have dramatically decreased with Cu and Si addition to the pure Ti sample. For example, the average length and width of the α-lath decreased from about 18.9 to 3.5 μm in pure Ti sample to about 3.3 and 1.7 μm in the Ti–5Cu–1Si sample, respectively (Fig. 12). Also, the average *GSF* of the α-laths changed from about 7.1 for the pure Ti sample to about 2.1 for the Ti–5Cu–1Si sample indicating the greater tendency of the latter for formation of equiaxed grains.

Previous investigations have discussed the decrease in the size of large grain-boundary and intragranular α colonies in the microstructure of Ti6Al4V-xB alloys in terms of three different phenomena occurring due to B addition, i.e. reduced prior β grain size which restricts the growth space of intragranular α phase, increased nucleation of α phase from defragmented α_{GB}, and formation of highly potent TiB substrates in the melt [31,49–51]. Following these findings, in the present work, the decrease in the size of α colonies and increased nucleation of α phase from defragmented α_{GB}, and the formation of highly potent TiB substrates in α-lath phases by Cu and Si addition to pure Ti can be related to the decrease in the size of the prior β grains.

3.2. Growth restriction factor (Q)

Maxwell et al. [52] have quantified the effect of constitutional supercooling of solute elements in binary alloys in terms of the *Q* factor. The value of *Q* is proportional to the rate at which a solute element can create ΔT_{CS} [11]. *Temp* - f_s curves for Ti–5Cu and Ti–1Si binary alloys based on equilibrium and non-equilibrium (Scheil) solidification conditions are shown in Fig. 13. The initial parts of ΔT_{CS}-f_s curves for Ti–5Cu and Ti–1Si binary alloys in Scheil non-equilibrium conditions and the second-order parabolic fit equations are shown in Fig. 14. Consequently, the growth restriction factor (Q_{true}) for Ti–5Cu and Ti–1Si alloys was obtained as 35 K and 25 K, respectively. Therefore, Q_{total} for Ti–5Cu–1Si alloy was obtained as about 60 K. According to the interdependence theory, the key factors that play a major role in grain refinement include the critical undercooling for nucleation (ΔT_n), ΔT_{CS} and the average spacing between the potent nucleation particles (x_{sd}) [53]. A small ΔT_n, large ΔT_{CS} and small x_{sd} result in the formation of an equiaxed microstructure. Larger *Q* values render more equiaxed grain nucleation. However, the small size of the laser-melted region, together with the high thermal gradient, significantly suppresses the extent of ΔT_{CS} zone formed in the L-PBF method and poses a challenge to achieve a fine grain size in Ti alloys [25]. It is postulated that Cu and Si addition to pure Ti leads to faster formation of ΔT_{CS} zone, which can effectively compensate for the negative effect of the high thermal gradient.

To signify the effects of Cu and Si on the microstructure and CET occurrence in Ti alloys, it is noteworthy that Al and V in Ti–6Al–4V alloy create a *Q* of only 8K, which is much lower than the ΔT_n during the solidification. As a result, wide columnar grains with an average width of 120 μm have been reported in AM Ti–6Al–4V alloy [54]. The addition of 12 wt% Mo to pure Ti increased the growth restriction factor to about 29 K, which did not significantly affect the formation of columnar grains, and columnar grains with lengths of 2 mm in the build direction were reported [31].

3.3. XRD analysis

X-ray diffraction (XRD) patterns of pure Ti, Ti–5Cu and Ti–5Cu–1Si samples are shown in Fig. 15(a). Most of the peaks are assigned to the α/α′ phase, but clearly, with the addition of Cu and Si, the β phase (110) peaks overlapping the α/α′ phase (002) peaks are also identified. Fig. 15

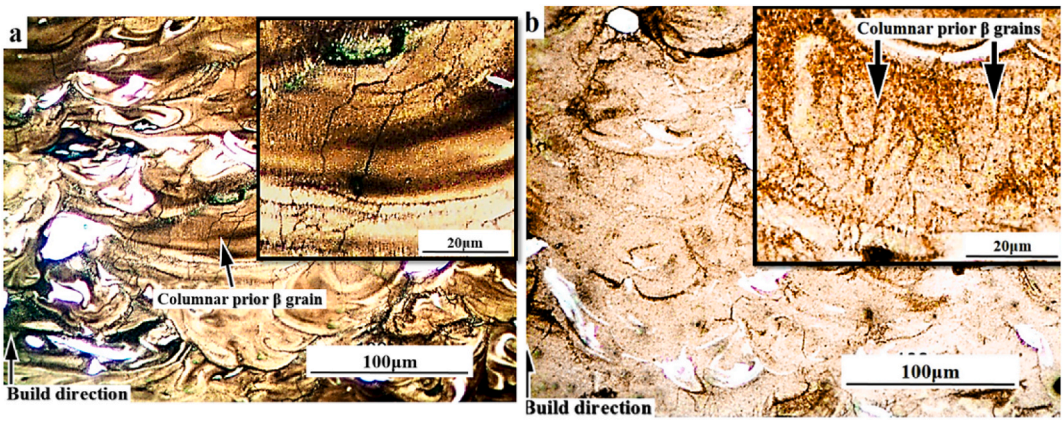

Fig. 9. Optical micrographs of Ti–5Cu–1Si sample at VED of a) 55.39 J/mm^3 and b) 64.63 J/mm^3.

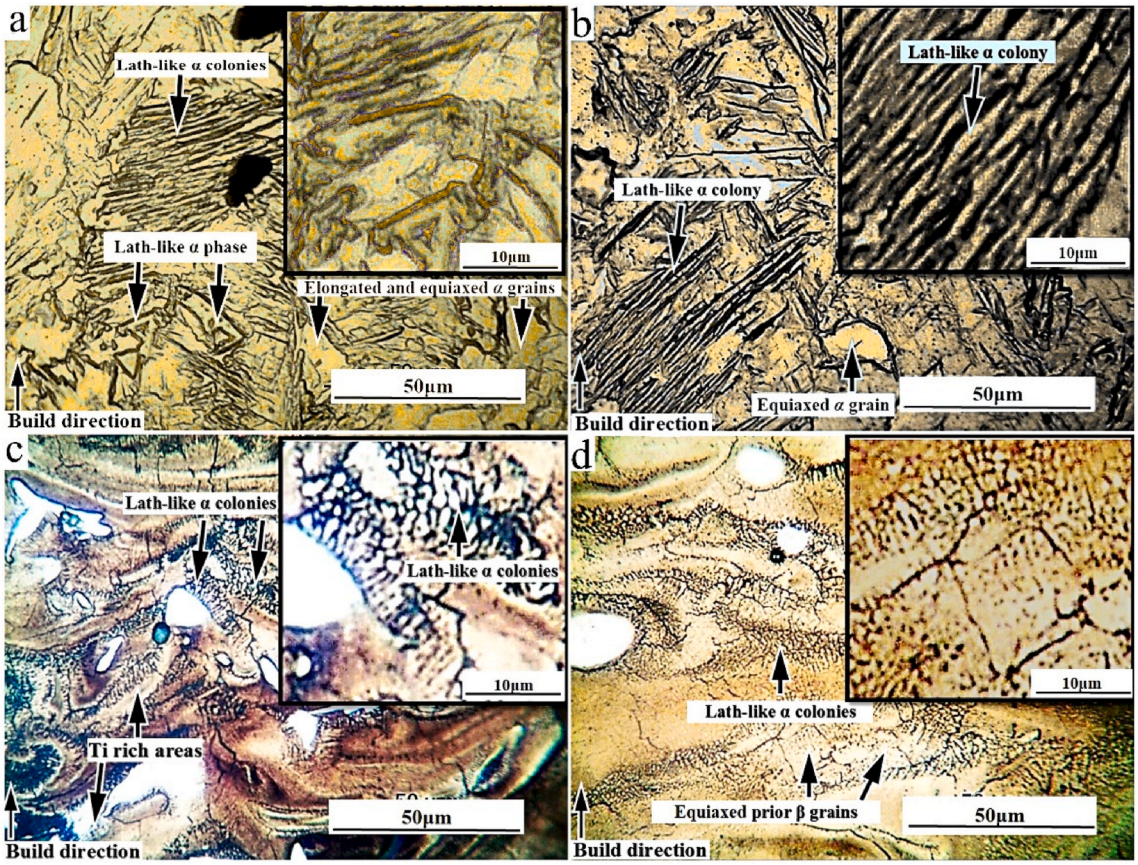

Fig. 10. OM micrographs of a) pure Ti sample (Y-Z cross-section), b) pure Ti sample (X-Z cross-section), c) Ti–5Cu–1Si sample (Y-Z cross-section) and d) Ti–5Cu–1Si sample (X-Z cross section) at VED of 50.26 J/mm^3.

(b) shows that all the peaks of the α/α′ phase are shifted to larger diffraction angles by Cu addition. With the introduction of Si, this shift towards larger angles becomes even more noticeable. This can be explained by considering the fact that guest atoms can be substituted in the Ti crystal lattice depending on their atomic size [12,55,56]. The atomic radius of Cu atoms (0.128 nm) and Si atoms (0.117 nm) are smaller than that of Ti atoms (0.147 nm) [12,55]. Therefore, by substituting Cu and Si atoms in the Ti HCP crystal lattice, the interplanar spacing of the crystal structure decreases, leading to a decrease in the *c/a* ratio of the Ti HCP structure. This explains the lattice microstrain behavior by Cu and Si addition in the Ti crystal lattice [12,55,57]. The atomic radius of Cu and Si is ~12% and ~20% smaller than that of Ti, respectively. Therefore, it is expected that Si can reduce the *c/a* ratio of the Ti HCP structure more than Cu and thus create a larger microstrain in the *α* lattice.

Fig. 16(a–c) shows Williamson-Hall plots for pure Ti, Ti–5Cu and Ti–5Cu –1Si samples. As it is evident from the figures, the slope of the Williamson-Hall diagrams increases from pure Ti to Ti–5Cu and Ti–5Cu–1Si samples, which represents the increase of lattice microstrain (Fig. 17(a)) due to the placement of Cu and Si elements in the Ti crystal lattice.

On the other hand, the lattice microstrain of the *α* phase is related to the crystal *c/a* ratio [24]. It can be seen in Fig. 17(b) that the *c/a* ratio of the HCP crystal lattice in the Ti–5Cu–1Si alloy has decreased much more

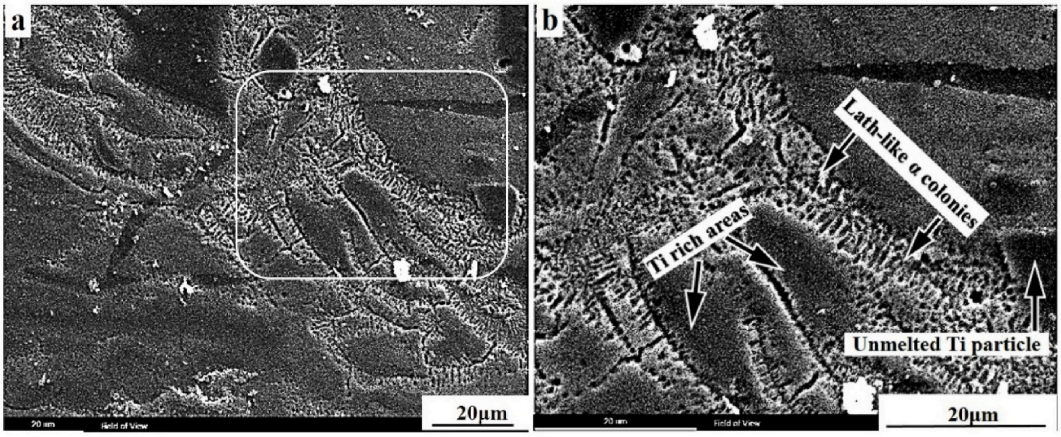

Fig. 11. a) SEM micrographs of Ti–5Cu–1Si sample at VED of 50.26 J/mm^3 and b) higher magnification of the selected area in (a).

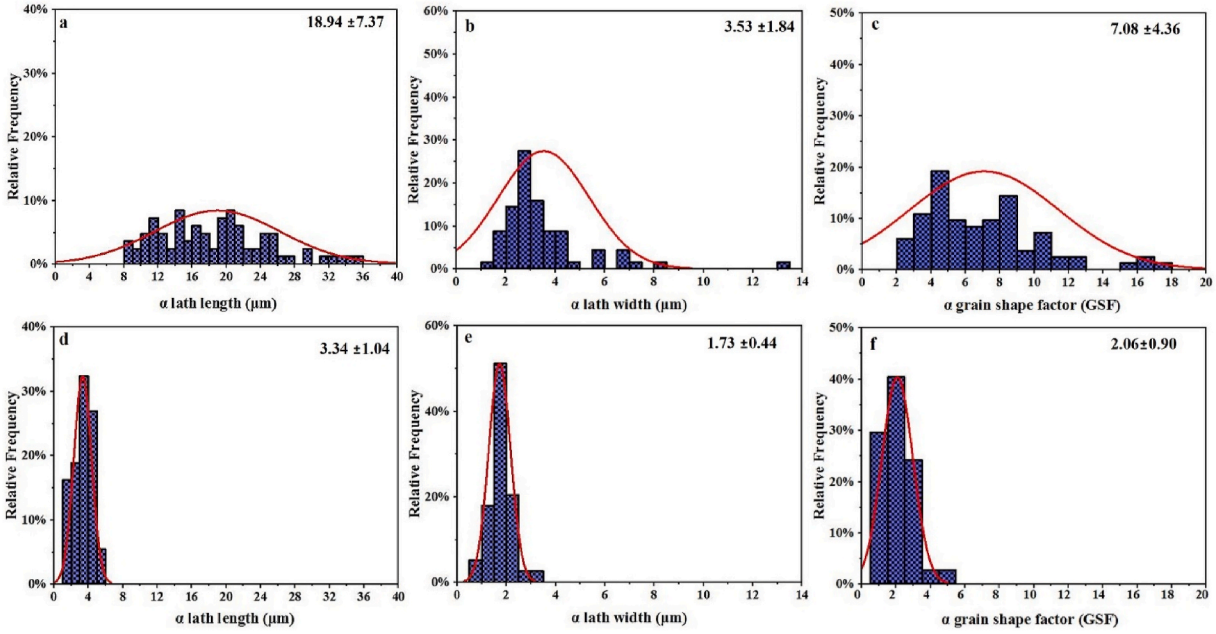

Fig. 12. Distribution histograms and the average value of a) length, b) width and c) *GSF* of the α-laths of the pure Ti sample and d) length, e) width and f) *GSF* of the α-laths of the Ti–5Cu–1Si sample at VED of 50.26 J/mm^3.

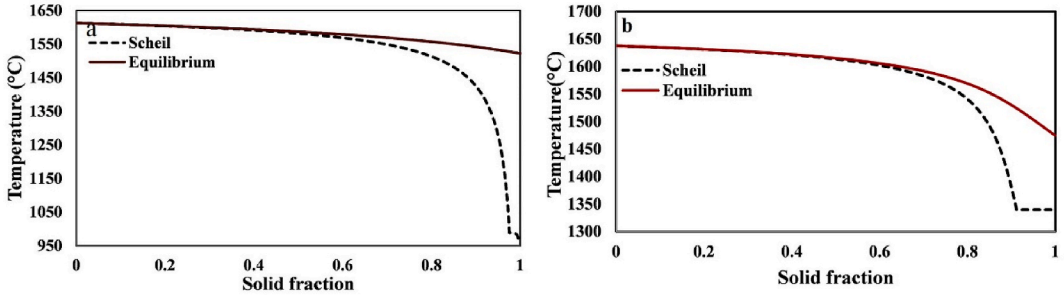

Fig. 13. Equilibrium and Scheil solidification curves of a) Ti–5Cu and b) Ti–1Si alloys.

than that of the Ti–5Cu alloy. In the XRD patterns (Fig. 15(a)), a broadening of the peak corresponding to the Ti–5Cu sample can be seen, which increases with the Si addition. This trend can be attributed to a decrease in the crystallite size of the α phase by Cu and Si addition. Fig. 17(c) shows that the crystallite size of the α phase for the Ti–5Cu sample is significantly smaller than that of the pure Ti sample. Si addition to the former, decreases the crystallite size of the α phase even further.

XRD spectra of different samples, as shown in Fig. 15(a), indicate a decrease in the intensity of the peaks from the pure Ti sample to the

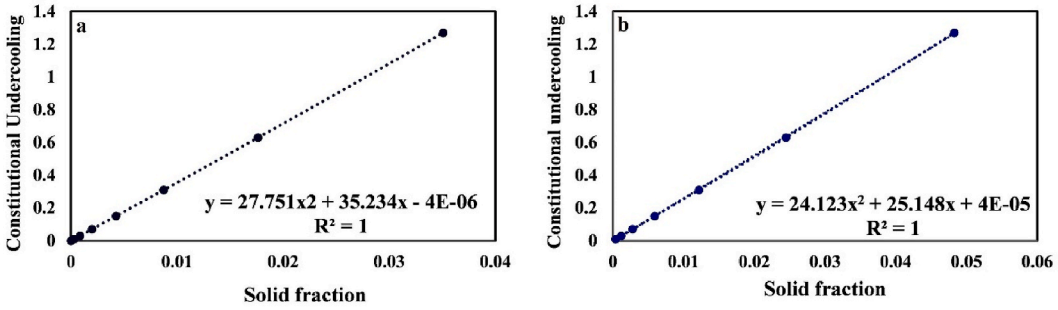

Fig. 14. Development of ΔT_{CS} with solid fraction for a) Ti–5Cu and b) Ti–1Si alloys.

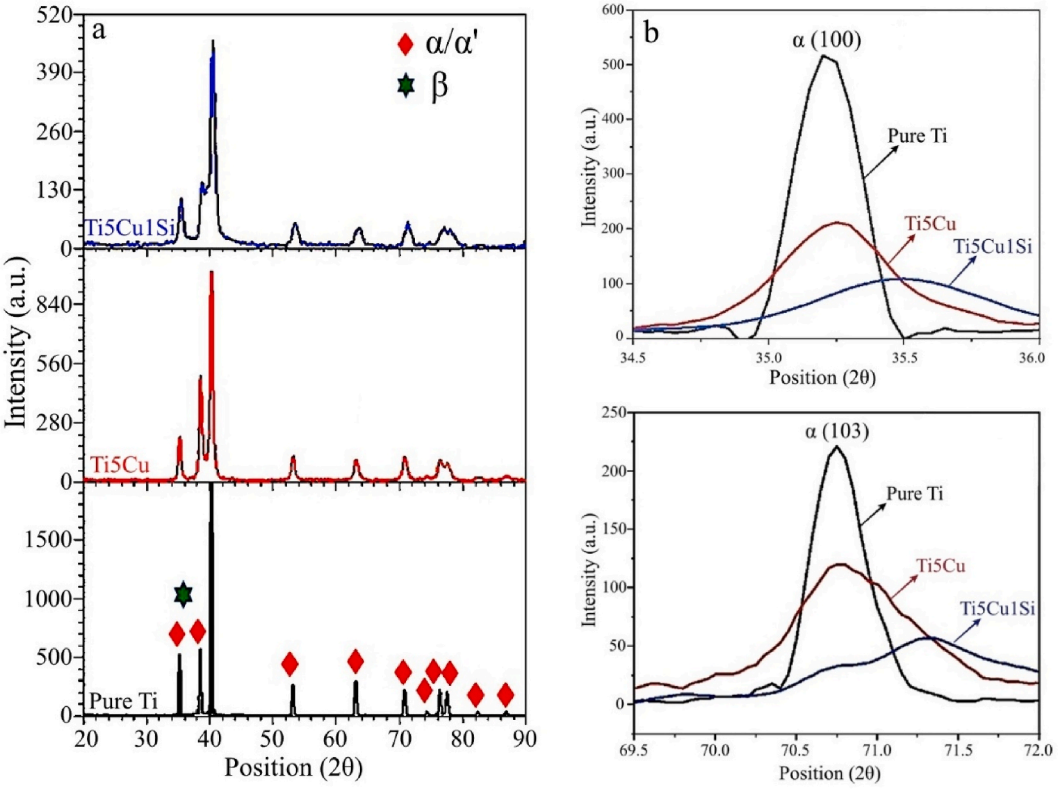

Fig. 15. a) XRD patterns of pure Ti, Ti–5Cu and Ti–5Cu–1Si samples and b) enlarged profiles of α (100) peak and α (103) peak.

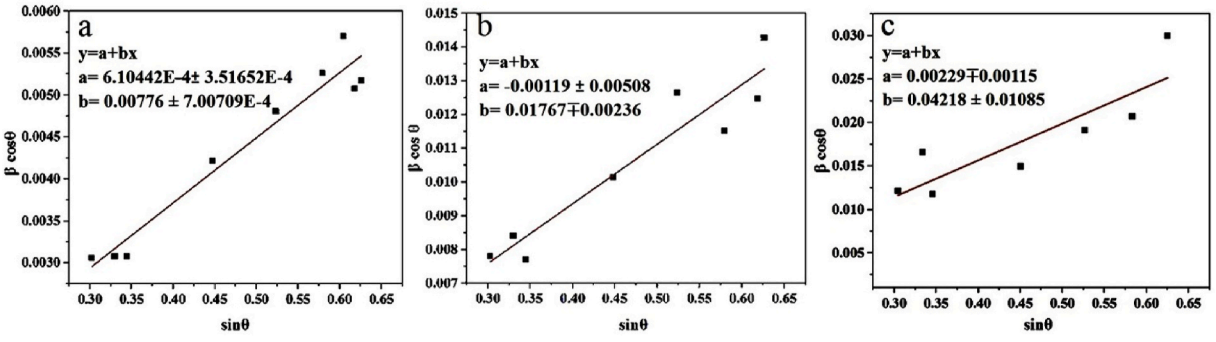

Fig. 16. Williamson-Hall plots for a) pure Ti, b) Ti–5Cu and c) Ti-5Cui -1Si specimens.

Ti–5Cu and the Ti–5Cu–1Si samples. This effect can be due to the reduction of the α phase by adding Cu and Si elements. By comparing the optical micrographs of different samples in Fig. 10(a–c), it is evident that Cu and Si elements have significantly changed the morphology and size of all types of α phases. Comparing the length, width and equivalent diameter of the α-laths in the microstructure of pure Ti with the

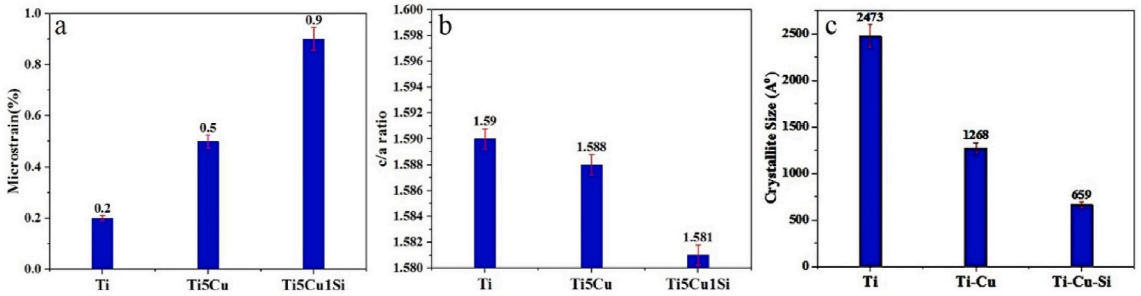

Fig. 17. Diagrams of a) α lattice microstrain, b) c/a ratio of the HCP lattice and c) α crystallite size of different samples.

Ti–5Cu–1Si sample (Fig. 12) confirms this reduction in the size of the α-laths by Cu and Si addition to pure Ti.

3.4. Relationship between growth restriction factor (Q) and microstructure

SEM micrographs of three microstructural areas of the Ti–5Cu–1Si sample printed using VED of 86.36 J/mm^3 and four area EDS analyses of the microstructure are shown in Fig. 18 to evaluate the relationship between the local grain size and local composition across the microstructure. It is evident that areas 2 and 4 in the microstructures encompass larger grains, while areas 1 and 3 include finer grains.

Fig. 19 displays the calculated ΔT_{CS} - f_s curves and the corresponding second-degree parabolic fit equations for Ti-xSi (x = 2.64, 2.85, 3.22, 4.56 wt%) and Ti-xCu (x = 11.42, 11.62, 11.76, 11.88 wt%) alloys conforming to the EDS analyses in Fig. 18. As can be seen, the Q parameter (b in $y = ax^2 + by + c$ equation) increases significantly as Cu and Si content increases. Graphs of Q as a function of Si and Cu contents are shown in Fig. 20, confirming that with increasing the Cu and Si contents, the grain size continuously decreases as a result of higher Q values (Fig. 20(c)). Higher Cu and Si contents would create steeper concentration profiles of Cu and Si in the liquid ahead of the solidification front, which yields a higher ΔT_{CS} and, therefore, triggers more nucleation events [58].

4. Conclusions

In the present investigation, the effect of in-situ alloying of Ti with Cu and Si by employing Laser Powder Bed Fusion (L-PBF) process was studied and their resultant microstructural evolution was systematically compared with that of pure titanium samples. This study delved into the intricate interplay between copper and silicon additions and the

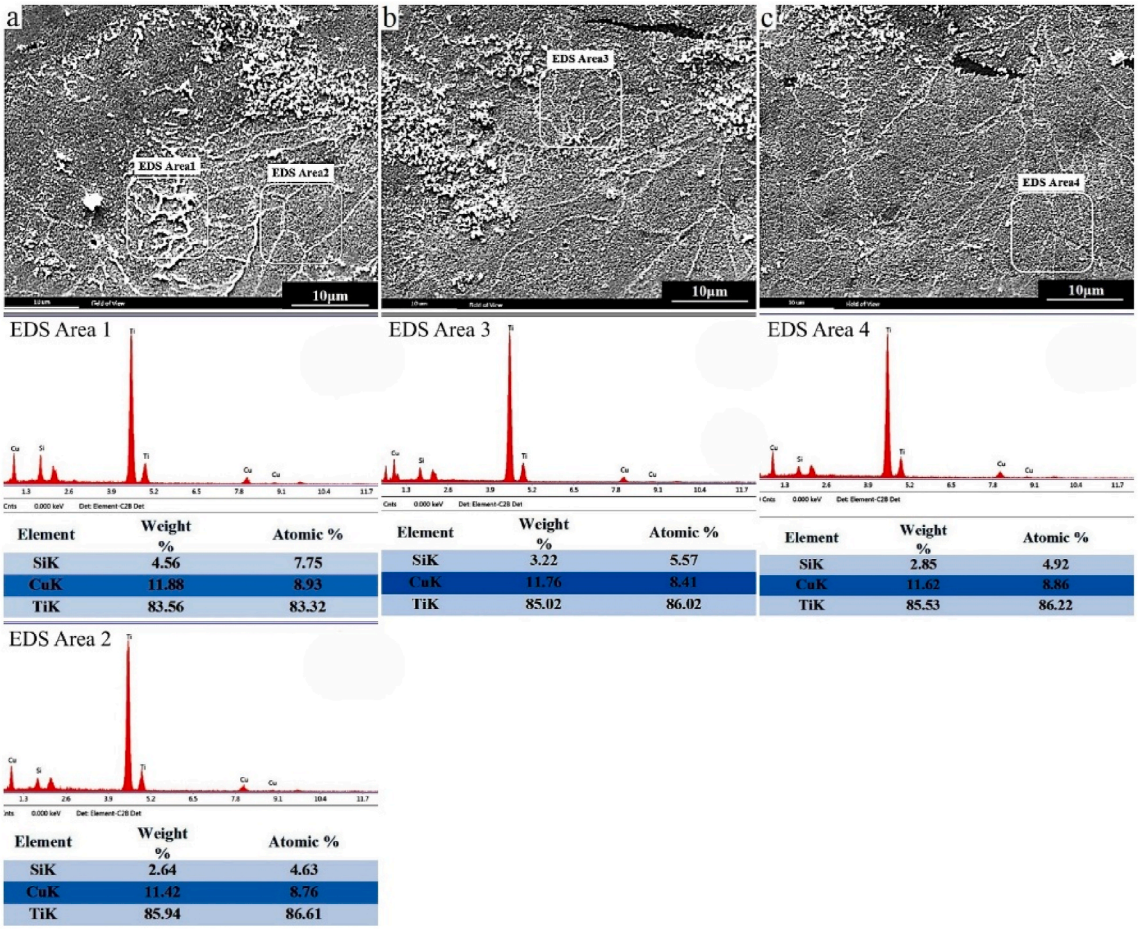

Element	Weight %	Atomic %
SiK	4.56	7.75
CuK	11.88	8.93
TiK	83.56	83.32

Element	Weight %	Atomic %
SiK	3.22	5.57
CuK	11.76	8.41
TiK	85.02	86.02

Element	Weight %	Atomic %
SiK	2.85	4.92
CuK	11.62	8.86
TiK	85.53	86.22

Element	Weight %	Atomic %
SiK	2.64	4.63
CuK	11.42	8.76
TiK	85.94	86.61

Fig. 18. SEM micrographs from several microstructural areas of Ti–5Cu–1Si sample at VED of 86.36 J/mm^3, and some related area EDS analyses.

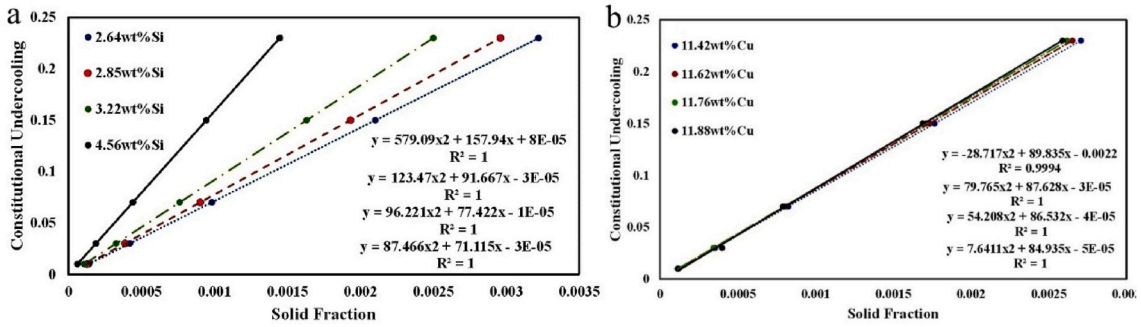

Fig. 19. Development of ΔT_{CS} - f_s for a) Ti-*X*.Si alloys (X = 2.64, 2.85, 3.22, 4.56 wt%) and b) Ti-*X*.Cu alloys (X = 11.42, 11.62, 11.76, 11.88 wt%).

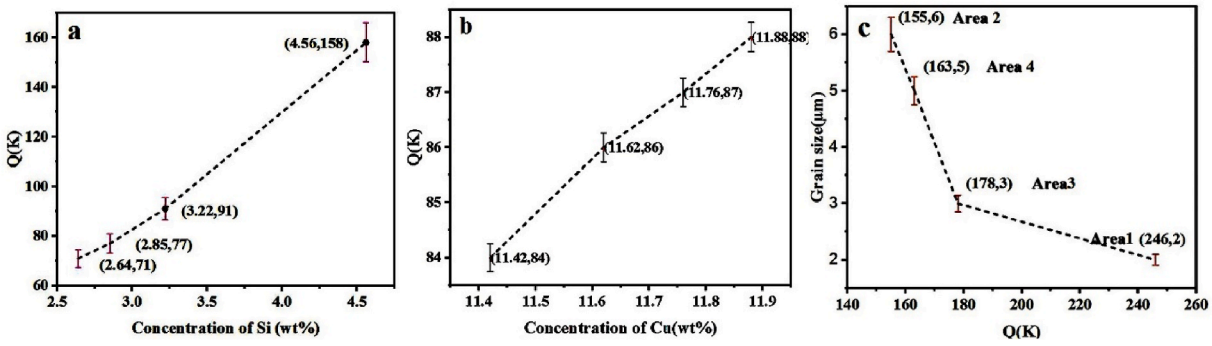

Fig. 20. *Q* as a function of a) Si content, b) Cu content and c) grain size in Ti–5Cu–1Si sample at VED of 86.36 J/mm^3.

consequential impact on microstructural characteristics while concurrently examining the influence of volumetric energy density. The ensuing conclusions drawn from the outcomes of this research are briefly outlined as follows.

F095 Cu addition induced the conversion of columnar β grains in the as-built pure Ti microstructure to equiaxed β grains in the as-built Ti–5Cu specimen.

F095 Si addition in Ti–5Cu–1Si samples resulted in an augmented number of smaller equiaxed β grains, contributing to refined microstructural characteristics.

F095 The combined influence of Cu and Si addition reduced the size of lath-like α phase colonies and decreased length, width, and aspect ratio of lath-like α in the Ti microstructure.

F095 Ti–5Cu–1Si alloy, characterized by an elevated volumetric energy density ranging from 50.26 to 86.36 J/mm^3, manifested an increased prevalence of uniform-sized β equiaxed grains.

F095 The Cu and Si addition decreased c/a ratio of the HCP crystal lattice in the as-built pure Ti samples, potentially escalating the lattice microstrain.

F095 A continuous decrease in crystallite size of the α phase was observed through Cu and Si addition, reflecting a progressive refinement in crystalline characteristics.

F095 Localized grain size reduction was achieved in the as-built state due to the segregation of Cu and Si, potentially resulting in a localized increase in *Q*.

F095 Localized increase in *Q* resulted in a continuous decrease in the grain size due to higher ΔT_{CS} formation and triggering of more nucleation events.

Declaration of competing interest

The authors declare that they have no known competing financial interests or personal relationships that could have appeared to influence the work reported in this paper.

References

[1] Zhang D, Sun S, Qiu D, Gibson MA, Dargusch MS, Brandt M, et al. Metal alloys for fusion-based additive manufacturing. Adv Eng Mater 2018;20:1700952. https://doi.org/10.1002/adem.201700952.

[2] Bolukbasi OS, Serindag TH, Gurol U, Gunen A, Cam G. Improving oxidation resistance of wire arc additive manufactured Inconel 625 Ni-based superalloy by pack aluminizing. CIRP J. Manuf. Sci. Technol. 2023;46:89–97. https://doi.org/10.1016/j.cirpj.2023.07.011.

[3] Gurol U, Altinay Y, Gunen A, Bolukbasi OS, Kocak M, Cam G. Effect of powder-pack aluminizing on microstructure and oxidation resistance of wire arc additively manufactured stainless steels. Surf Coating Technol 2023;468:129742. https://doi.org/10.1016/j.surfcoat.2023.129742.

[4] Gunen A, Gurol U, Kocak M, Cam G. Investigation into the influence of boronizing on the wear behavior of additively manufactured Inconel 625 alloy at elevated temperature. Progress in Additive Manufacturing 2023;8:1281–301. https://doi.org/10.1007/s40964-023-00398-8.

[5] Taghian M, Mosallanejad MH, Lannunziata E, Del Greco G, Iuliano L, Saboori A. Laser powder bed fusion of metallic components: latest progress in productivity, quality, and cost perspectives. J Mater Res Technol 2023;27:6484–500. https://doi.org/10.1016/j.jmrt.2023.11.049.

[6] Mosallanejad MH, Abdi A, Karpasand F, Nassiri N, Iuliano L, Saboori A. Additive manufacturing of titanium alloys; processability, properties and applications. Adv Eng Mater 2023;2301122:1–29.

[7] Dadkhah M, Mosallanejad MH, Iuliano L, Saboori A. A comprehensive overview on the latest progress in the additive Manufacturing of metal matrix composites: potential, challenges and feasible solutions. Acta Metall Sin 2021;34:1173–200. https://doi.org/10.1007/s40195-021-01249-7.

[8] Mosallanejad MH, Niroumand B, Aversa A, Saboori A. In-situ alloying in laser-based additive manufacturing processes: a critical review. J Alloys Compd 2021; 872:159567. https://doi.org/10.1016/j.jallcom.2021.159567.

[9] Saboori A, Abdi A, Fatemi SA, Marchese G, Biamino S, Mirzadeh H. Hot deformation behavior and flow stress modeling of Ti–6Al–4V alloy produced via electron beam melting additive manufacturing technology in single β-phase field. Mater Sci Eng, A 2020;792:139822. https://doi.org/10.1016/j.msea.2020.139822.

[10] Galati M, Defanti S, Saboori A, Rizza G, Tognoli E, Vincenzi N, et al. An investigation on the processing conditions of Ti-6Al-2Sn-4Zr-2Mo by electron beam powder bed fusion, microstructure, defect distribution, mechanical properties and dimensional accuracy. Addit Manuf 2022;50:102564. https://doi.org/10.1016/j.addma.2021.102564.

[11] Collins PC, Brice DA, Samimi P, Ghamarian I, Fraser HL. Microstructural control of additively manufactured metallic materials. Annu Rev Mater Res 2016;46:63–91. https://doi.org/10.1146/annurev-matsci-070115-031816.

[12] Mosallanejad MH, Niroumand B, Ghibaudo C, Biamino S, Salmi A, Fino P, et al. In-situ alloying of a fine grained fully equiaxed Ti-based alloy via electron beam

powder bed fusion additive manufacturing process. Addit Manuf 2022;56:102878. https://doi.org/10.1016/j.addma.2022.102878.
[13] Lun C, Leung A, Tosi R, Muzangaza E, Nonni S, Withers PJ, et al. Effect of preheating on the thermal, microstructural and mechanical properties of selective electron beam melted Ti-6Al-4V components. Mater Des 2019;174:107792. https://doi.org/10.1016/j.matdes.2019.107792.
[14] Carroll BE, Palmer TA, Beese AM. Anisotropic tensile behavior of Ti–6Al–4V components fabricated with directed energy deposition additive manufacturing. Acta Mater 2015;87:309–20. https://doi.org/10.1016/j.actamat.2014.12.054.
[15] Yuan L, Sabau AS, StJohn D, Prasad A, Lee PD. Columnar-to-equiaxed transition in a laser scan for metal additive manufacturing. Mater Sci Eng 2020;861:012007. https://doi.org/10.1088/1757-899X/861/1/012007.
[16] Xu W, Lui EW, Pateras A, Qian M, Brandt M. In situ tailoring microstructure in additively manufactured Ti-6Al-4V for superior mechanical performance. Acta Mater 2017;125:390–400. https://doi.org/10.1016/j.actamat.2016.12.027.
[17] Prasad A, Yuan L, Lee P, Patel M, Qiu D, Easton M, et al. Towards understanding grain nucleation under additive manufacturing solidification conditions. Acta Mater 2020;195:392–403. https://doi.org/10.1016/j.actamat.2020.05.012.
[18] Bermingham MJ, StJohn DH, Krynen bJ, Tedman-Jones S, Dargusch MS. Promoting the columnar to equiaxed transition and grain refinement of titanium alloys during additive manufacturing. Acta Mater 2019;168:261–74. https://doi.org/10.1016/j.actamat.2019.02.020.
[19] Fan Z, Gao F, Zhou L, Lu SZ. A new concept for growth restriction during solidification. Acta Mater 2018;152:248–57. https://doi.org/10.1016/j.actamat.2018.04.045.
[20] Bermingham M, Stjohn D, Easton M, Yuan L, Dargusc M. Revealing the mechanisms of grain nucleation and formation during additive manufacturing. Jom 2020;72:1065–73. https://doi.org/10.1007/s11837-020-04019-5.
[21] Schmid-Fetzer R, Kozlov A. Thermodynamic aspects of grain growth restriction in multicomponent alloy solidification. Acta Mater 2011;59:6133–44. https://doi.org/10.1016/j.actamat.2011.06.026.
[22] Vilardell AM, Takezawa A, du Plessis A, Takata N, Krakhmalev P, Kobashi M, et al. Mechanical behavior of in-situ alloyed Ti6Al4V(ELI)-3 at.% Cu lattice structures manufactured by laser powder bed fusion and designed for implant applications. J Mech Behav Biomed Mater 2021;113:104130. https://doi.org/10.1016/j.jmbbm.2020.104130.
[23] Krakhmalev P, Yadroitsev I, Yadroitsava I, Smidt Od. Functionalization of biomedical Ti6Al4V via in Situ alloying by cu during laser powder bed fusion manufacturing. Materials 2017;10:1154. https://doi.org/10.3390/ma10101154.
[24] Mosallanejad MH, Niroumand B, Aversa A, Manfredi D, Saboori A. Laser powder bed fusion in-situ alloying of Ti-5%Cu alloy: process-structure relationships. J Alloys Compd 2021;857:157558. https://doi.org/10.1016/j.jallcom.2020.157558.
[25] Zhang D, Qiu D, Gibson MA, Zheng Y, Fraser HL, StJohn DH, et al. Additive manufacturing of ultrafine-grained high-strength titaniumalloys. Nature 2019;576:91–5. https://doi.org/10.1038/s41586-019-1783-1.
[26] Mereddy S, Bermingham MJ, StJohn DH, Dargusch MS. Grain refinement of wire arc additively manufactured titanium by the addition of silicon. J Alloys Compd 2017;695:2097–103. https://doi.org/10.1016/j.jallcom.2016.11.049.
[27] Guercio GD, Galati M, Saboori A, Fino P, Iuliano L. Microstructure and mechanical performance of Ti–6Al–4V lattice structures manufactured via electron beam melting (EBM): a review. Acta Metall Sin (Engl Lett) 2020;33:183–203. https://doi.org/10.1007/s40195-020-00998-1.
[28] Gepreel AH, Niinomi M. Biocompatibility of Ti-alloys for longterm implantation. J. Mech. Behav. Biomed 2013;20:407–15. https://doi.org/10.1016/j.jmbbm.2012.11.014.
[29] Xu X, Lu Y, Li S, Guo S, He M, Luo K, et al. Copper-modified Ti6Al4V alloy fabricated by selective laser melting with pro-angiogenic and anti-inflammatory properties for potential guided bone regeneration applications. Mater Sci Eng C 2018;90:198–210. https://doi.org/10.1016/j.msec.2018.04.046.
[30] Zhang F, Mei M, Al-Hamdani K, Tan H, Clare AT. Novel nucleation mechanisms through satelliting in direct metal deposition of Ti-15Mo. Mater Lett 2018;213:197–200. https://doi.org/10.1016/j.matlet.2017.11.036.
[31] Mantri SA, Alam T, Choudhuri D, Yannetta CJ, Mikler CV, Collins PC, et al. The effect of boron on the grain size and texture in additively manufactured β-Ti alloys. J Mater Sci 2017;48:1–22. https://doi.org/10.1007/s10853-017-1371-4.
[32] Mendoza M, Smimi P, Brice D, Martin BW, Rolchigo MR, Lesar R, et al. Microstructures and grain refinement of additive-manufactured Ti-xW alloys. Metall Mater Trans A 2017;48:1–12. https://doi.org/10.1007/s11661-017-4117-7.
[33] Luo J, Guo S, Lu Y, Xu X, Zhao C, Wu S, et al. Cytocompatibility of cu-bearing Ti6Al4V alloys manufactured by selective laser melting. Mater. Charact 2017;143:127–36. https://doi.org/10.1016/j.matchar.2017.12.003.
[34] Choi G, Choi WS, Han J, Choi PP. Additive manufacturing of titanium-base alloys with equiaxed microstructures using powder blends. Addit Manuf 2020;36:101467. https://doi.org/10.1016/j.addma.2020.101467.
[35] Mosallanejad MH. Investigating effective solidification mechanisms in in-situ manufacturing of titanium-based alloys by additive manufacturing method based on powder bed [P.hd. dissertation]. Isfahan University of Technology; 2022.
[36] Kim YY, Schenk AS, Ihli J, Kulak AN, Hetherington NBJ, Tang CC, et al. A critical analysis of calcium carbonate mesocrystals. Nat Commun 2014;5:4341. https://doi.org/10.1038/ncomms5341.
[37] Mesbah M, Faraji G, Bushroa AR. Characterization of nanostructured pure aluminum tubes produced by tubular channel angular pressing (TCAP). Mater Sci Eng 2014;590:289–94. https://doi.org/10.1016/j.msea.2013.10.036.
[38] Beal M, Azzougagh MN, Pourchez J, Bertrand P, Cabrol E, Mohand H, et al. Effect of powder reuse on physical, chemical and toxicological properties of 6061-Zr aluminum alloy processed by laser powder bed fusion (L-PBF). Matériaux Tech 2023;111:1–16. https://doi.org/10.1051/mattech/2023013.
[39] Liu S, Shin YC. Additive manufacturing of Ti6Al4V alloy: a review. Mater Des 2019;164:107552. https://doi.org/10.1016/j.matdes.2018.107552.
[40] Wysocki B, Maj P, Krawczynska A, Zdunek J, Rozniatowski K, Kurzydłowski KJ, et al. Microstructure and mechanical properties investigation of CP Titanium processed by selective laser melting (SLM). J Mater Process Technol 2016;241:13–23. https://doi.org/10.1016/j.jmatprotec.2016.10.022.
[41] Li XP, Humbeeck JV, Krutha JP. Selective laser melting of weak-textured commercially pure titanium with high strength and ductility: a study from laser power perspective. Mater Des 2016;116:352–8. https://doi.org/10.1016/j.matdes.2016.12.019.
[42] Zhang B, Liao H, Coddet C. Microstructure evolution and density behavior of CP Ti parts elaborated by Self-developed vacuum selective laser melting system. Appl Surf Sci 2013;279:310–6. https://doi.org/10.1016/j.apsusc.2013.04.090.
[43] Yi M. A complete guide to violin plots, tutorial by chartio. Available from: https://chartio.com/learn/charts/violin-plot-complete-guide/; 2022.
[44] Sun M, StJohn DH, Easton MA, Wang K, Ni J. Effect of cooling rate on the grain refinement of Mg-Y-Zr alloys. Metall Mater Trans A 2019;51:482–96. https://doi.org/10.1007/s11661-019-05497-2.
[45] Naoki D, Yamamoto NS, Watanabe Y, Sato H, Nakano S, Sato N, et al. Effects of solidification conditions on grain refinement capacity of TiC in directionally solidified Ti6Al4V alloy. Metall Mater Trans A 2021;52:1–19. https://doi.org/10.1007/s11661-021-06333-2.
[46] Liotti E, Arteta C, Zisserman A, Lui A, Lempitsky V, Grant PS. Crystal nucleation in metallic alloys using x-rayradiography and machine learning. Sci Adv 2018;4:1–9. https://doi.org/10.1126/sciadv.aar4004.
[47] Yadroitsev I, Krakhmalev P, Yadroitsava I. Titanium alloys manufactured by in situ alloying during laser powder bed fusion. JOM 2017;69:2725–30. https://doi.org/10.1007/s11837-017-2600-7.
[48] Vilardell AM, Yadroitsev I, Yadroitsava I, Krakhmalev P, Kouprianoff D, Kothleitner G, et al. Manufacturing and characterization of in-situ alloyed Ti6Al4V (ELI)-3 at.% Cu by Laser powder bed fusion. Addit Manuf 2020;36:1–29. https://doi.org/10.1016/j.addma.2020.101436.
[49] Xue A, Wang L, Lin X, Wang J, Chen J, Huang W. Effect of boron on the microstructure and mechanical properties of Ti-6Al-4V produced by laser directed energy deposition after heat treatment. J Laser Appl 2020;32:012007. https://doi.org/10.2351/1.5098074.
[50] Xue A, Lin X, Wang L, Wang J, Huang W. Influence of trace boron addition on microstructure, tensile properties and their anisotropy of Ti6Al4V fabricated by laser directed energy deposition. Mater Des 2019;181:107943. https://doi.org/10.1016/j.matdes.2019.107943.
[51] Zhang K, Tian X, Bermingham M, Rao J, Jia Q, Zhu Y, et al. Effects of boron addition on microstructures and mechanical properties of Ti-6Al-4V manufactured by direct laser deposition. Mater Des 2019;184:108191. https://doi.org/10.1016/j.matdes.2019.108191.
[52] Maxwell I, Hellawell A. A simple model for grain refinement during solidification. Acta 1975;23:229–37. https://doi.org/10.1016/0001-6160(75)90188-1.
[53] StJohn DH, Qian M, Easton MA, Cao P. The Interdependence Theory: the relationship between grain formation and nucleant selection. Acta Mater 2011;59:4907–21. https://doi.org/10.1016/j.actamat.2011.04.035.
[54] Yin B, Ma H, Wang J, Fang K, Zhao H, Liu Y. Effect of CaF 2 addition on macro/microstructures and mechanical properties of wire and arc additive manufactured Ti-6Al-4V components. Mater Lett 2017;190:64–6. https://doi.org/10.1016/j.matlet.2016.12.128.
[55] Oh JM, Lim JW, Lee BG, Suh CY, Cho SW, Lee SW, et al. Grain refinement and hardness increase of titanium via trace element addition. Metall Mater Trans 2010;51:2009–12. https://doi.org/10.2320/matertrans.M2010175.
[56] Khairallah SA, Anderson AT, Rubenchik A, King WE. Laser powder-bed fusion additive manufacturing: physics of complex melt flow and formation mechanisms of pores, spatter, and denudation zones. Acta Mater 2016;108:36–45. https://doi.org/10.1016/j.actamat.2016.02.014.
[57] Simbi DJ, Scully JC. The effect of residual interstitial elements and iron on mechanical properties of commercially pure titanium. Mater Lett 1996;26:35–9. https://doi.org/10.1016/0167-577X(95)00204-9.
[58] Wang M, Ma Z, Xu Z, Cheng XW. Designing Vx NbMoTa refractory high-entropy alloys with improved properties for high-temperature applications. Scripta Mater 2021;191:131–6. https://doi.org/10.1016/j.scriptamat.2020.09.027.